SCIENCE CHINA
Physics, Mechanics & Astronomy

• Article •

October 2021 Vol. 64 No. 10: 104211
https://doi.org/10.1007/s11433-021-1767-5

# Generation and control of dynamically tunable circular Pearcey beams with annular spiral-zone phase

KaiHui Chen[1,2†], HuiXin Qiu[1,2†], You Wu[1,2], ZeJia Lin[1,2], HaiQi Huang[1,2], LingLing Shui[1,2], DongMei Deng[1,2*], HongZhan Liu[1,2*], and ZhiGang Chen[3*]

[1] *Guangdong Provincial Key Laboratory of Nanophotonic Functional Materials and Devices, South China Normal University, Guangzhou 510631, China;*
[2] *School of Information and Optoelectronic Science and Engineering, South China Normal University, Guangzhou 510006, China;*
[3] *MOE Key Laboratory of Weak-Light Nonlinear Photonics, TEDA Applied Physics Institute and School of Physics, Nankai University, Tianjin 300457, China*

Received June 5, 2021; accepted August 16, 2021; published online August 26, 2021

Light-field shaping technology plays an important role in optics and nanophotonics. For instance, the spatially structured light field, which exhibits characteristic features in complex phases, light intensity, and polarization, is crucial to understanding new physical phenomena and exploring practical applications. Herein, we propose and demonstrate a new class of tunable circular Pearcey beams (TCPBs) by imposing the annular spiral-zone phase (ASZP). Through experiments, we used a spatial light modulator to generate TCPBs based on their spiral phase distribution, and numerically analyzed the generation and control of the beams with unusual autofocusing and self-rotating dynamics. ASZP is a general term for complex phases composed of the spiral phase, equiphase, and radial phase. TCPB typically exhibits dynamical properties, including abrupt autofocusing, automatic generation of optical bottles, and self-rotation of the beam pattern, during propagation. Besides, the number of generated optical bottles can be modulated by the superposition mode of ASZP and the number of subphases. We found that an inappropriate superposition mode leads to distortion, and we analyzed the underlying mechanism. Potential applications of TCPBs in optical manipulation are also discussed, presenting an exemplary role desired for light-field manipulation.

**annular spiral-zone phases, abruptly autofocusing beams, optical bottles**

**PACS number(s):** 41.85.Ct, 41.85.Lc, 42.25.Bs

**Citation:** K. H. Chen, H. X. Qiu, Y. Wu, Z. J. Lin, H. Q. Huang, L. L. Shui, D. M. Deng, H. Z. Liu, and Z. G. Chen, Generation and control of dynamically tunable circular Pearcey beams with annular spiral-zone phase, Sci. China-Phys. Mech. Astron. **64**, 104211 (2021), https://doi.org/10.1007/s11433-021-1767-5

## 1 Introduction

The Pearcey function was discovered in 1946 by Pearcey [1] through analytical derivation and numerical calculation of field structures at and near the focal line of a cylindrical electromagnetic wave. In 2012, Ring et al. [2] introduced the Pearcey function into optics and realized Pearcey beams through theoretical and experimental studies. Pearcey beams represent a solution of the paraxial equation and describe

*Corresponding authors (DongMei Deng, email: dmdeng@263.net; HongZhan Liu, email: lhzscnu@163.com; ZhiGang Chen, email: zgchen@nankai.edu.cn)
†These authors contributed equally to this work.

diffraction near two-dimensional caustics [3], which have the same self-healing and -focusing properties as Airy beams during propagation. To date, different forms of Pearcey beams have been proposed. Among them, circle Pearcey beams [4] have attracted extensive attention owing to their abruptly autofocusing (AAF) properties, including high peak intensity contrast, short focal length, and no oscillation after focusing. Several new designs based on circle Pearcey beams, including chirp ring Pearcey beams [5], vector ring Pearcey beams [6], ring Pearcey beams with a cross-phase [7], and generalized ring Pearcey beams [8], have also been proposed.

The AAF properties of circular Airy beams were first reported by Efremidis et al. [9] and later verified experimentally [10, 11]. AAF beams possess a large focal depth and a small divergence angle, which play an important role in increasing the power density of the beams. Compared to conventional Gaussian beams, when AAF beams are propagated, the interaction between the beams and the media diminishes, and even disappears, before focusing so that they can focus on target positions. Besides, their profiles turn into a Bessel-like pattern soon after abrupt focusing [11], preventing damage during subsequent propagation through the media. Therefore, AAF beams are vital in laser processing and biomedical treatment [9, 12]. Moreover, their applications have been extended to optical trapping [11], atom manipulation [13], etc. On the other hand, AAF beams have a symmetrical caustic distribution and form a large gradient light field that can capture and simultaneously manipulate particles. Therefore, AAF beams have attracted significant interest recently [14]. For example, Panagiotopoulos et al. [15] reshaped AAF beams into nonlinear intense light-bullet wave packets, which have significant advantages in attosecond physics. Jiang et al. [16] used AAF beams to capture two types of particles in the area of particle manipulation. Simultaneously, nonparaxial autofocusing beams with preengineered trajectories associated with larger intensity contrasts, focusing at smaller distances and smaller spot sizes as compared with the paraxial case, have been investigated [17].

In theory, if AAF beams focus more than twice, they are likely to form optical bottles (OBs) [18, 19]. OB is an optical field possessing a dark closed region and offers an optical trap in three dimensions. OB beams, which can trap aerosol particles [20] and low-refractive-index particles compared with the traditional convergent Gaussian beams, have unique applications in optical tweezers. OB was first demonstrated by Arlt and Padgett [18] by superimposing vortex beams. It was obtained by various methods, including self-image effect [21], Fourier-space generation [22], and caustics under revolution [23]. Although optical cages employ similar optical traps in three dimensions as OBs, they are mainly generated by vector beams, and some are even generated in numerical-aperture optical systems [24-27]. In addition, an optical vortex (OV) beam is a spatially structured light field widely used in optical tweezers, and it has the characteristics of spiral phase distribution, phase singularity, and zero central light intensity. OV beams have a certain orbital angular momentum (OAM) [28]. Since the zero intensity in the axial region of OV weakens the scattering force, as opposed to the gradient force, OV can capture particles with both high and low refractive indices [29]. Furthermore, OV can transfer the OAM of a beam to particles, driving them to rotate like an optical spinner [30-34].

Recently, with the in-depth exploration of vortex beams, traditional vortex beams no longer meet the application needs. Multiple new light fields with special light field distribution based on the modulation of phases, amplitudes, and polarization have been proposed [35]. Ni et al. [36] formed a 3D spiral light field through coaxial coherence between a vortex beam and a plane wave. The spiral light-field implements a 3D spiral chiral nanostructure with a 3D twisted cross-section in an isotropic material. In addition, a new phase modulation, imposing the annular spiral-zone phase (ASZP) on a beam phase, was proposed by Lan et al. [37] to generate tunable polycyclic chiral Gaussian beams. In this method, the superposition between an equiphase and a spiral phase is equivalent to the interference between a vortex beam and a plane wave. Then, Wu et al. [38] theoretically proposed a polycyclic tornado ring Airy beam induced by ASZP with the second-order chirped factor and analyzed its AAF characteristics. However, the propagation properties of tunable circular Pearcey beams (TCPBs), circle Pearcey beams produced with ASZP, have not been reported.

In this study, we derive theoretically and demonstrate experimentally TCPBs. Additionally, the properties of the beams, such as AAF, automatic generation of OBs, and self-rotation of the beam pattern, are analyzed. In sect. 2, we illustrate the theoretical model and propagation dynamics of TCPBs and highlight the influence of the number of subphase and annular phases for the TCPBs to discuss the propagation properties of TCPBs. In sect. 3, the experimental setup and results are presented. In sect. 4, we summarize the results of the study.

## 2 Theoretical model and propagation dynamics of TCPBs

### 2.1 Theory

In paraxial optical systems, the (2+1)-dimensional normalized potential-free Schrödinger equation describes the spatial

beam dynamics while propagating along $z$-axis. In terms of the radially symmetrical beam solution, TCPBs can be expressed more easily in cylindrical coordinates as [4,9]:

$$2\mathrm{i}\frac{\partial E}{\partial z}+\frac{\partial^2 E}{\partial r^2}+r^{-1}\frac{\partial E}{\partial r}+r^{-2}\frac{\partial^2 E}{\partial \theta^2}=0, \tag{1}$$

where $E(r,\theta,z)$ is the amplitude of TCPBs, and $(r,\theta)$ is the polar coordinates. The radial distance $r$ is normalized with arbitrary transverse length $x_0$, the propagation distance $z$ is normalized with $k{x_0}^2$, and $k=2\pi/\lambda_0$ ($\lambda_0$ is the center wavelength in free space) represents the wavenumber.

The initial optical field of TCPBs imposed with ASZP can be expressed in cylindrical coordinates as:

$$E(r,\theta,0)=A_0 Pe(-r/p_\mathrm{s},0)q(r)\exp\left[\mathrm{i}\Phi(r,\varphi)\right], \tag{2}$$

where $A_0$ is the normalized constant amplitude of the initial optical field, and $Pe(\cdot)$ is the Pearcey integral [1,2] in terms of $Pe(s,t)=\int_{-\infty}^{+\infty}\mathrm{d}q\exp\left(\mathrm{i}q^4+\mathrm{i}q^2t+\mathrm{i}qs\right)$. The spatial distribution factor $p_\mathrm{s}$ can manipulate the intensity distribution of the input beams and the position of the focal point (i.e., the focal length $L_\mathrm{s}=2p_\mathrm{s}^2$) [4]. Ideally, the light fields of TCPBs and other Pearcey beams are distributed in an infinite space [1]. $q(r)$ guarantees that the total conveyed power $\int_0^{2\pi}\int_0^{\infty}E\left(r,\theta,0\right)\mathrm{d}r\mathrm{d}\theta$ is finite. To experimentally generate TCPBs, it can be described as:

$$q(r)=\begin{cases}\mathrm{e}^{\eta r^{\xi}}, & r<r_0,\\ 0, & r\geq r_0,\end{cases} \tag{3}$$

and $\eta$, $\xi$ can adjust the amplitude distribution of the input beams at $r<r_0$. ASZP $\Phi(r,\varphi)$ is composed of multiple subphases $\phi_i(r,\varphi)$, which is defined as ASZP$n$, with $n$ corresponding to the number of subphases. The phase distribution of ASZP can be expressed as [37]:

$$\Phi\left(r,\varphi\right)=\sum_{i=1}^{n}\mathrm{circ}\left(\frac{r}{r_\mathrm{max}}\right)\phi_i\left(r,\varphi\right), \tag{4}$$

where $\mathrm{circ}(r/r_\mathrm{max})$ is the cylindrical function. Figure 1(a1) depicts the structure of the subphases. Every subphase contains three annular phases, including the radial phase, equiphase, and spiral phase, starting from the inner part of the phase distribution, which can be expressed as [37,39]:

$$\phi_i(r,\varphi)=\begin{cases}\beta r, & r_i^{\mathrm{ir}}<r<r_i^{\mathrm{or}},\\ \gamma, & r_i^{\mathrm{ie}}<r<r_i^{\mathrm{oe}},\\ l_i\varphi+\alpha r, & r_i^{\mathrm{is}}<r<r_i^{\mathrm{os}},\end{cases} \tag{5}$$

where $\beta r$, $\gamma$ and $l_i\varphi+\alpha r$ denote the radial phase, equiphase, and spiral phase of the $i$th subphase, respectively; $l_i$ represents the topological charge for the $i$th subphase; $\alpha$ and $\beta$ are the tunable radial shift factors. $r_i^{\mathrm{ir}}$, $r_i^{\mathrm{ie}}$, and $r_i^{\mathrm{is}}$ are the inner radii of the $i$th radial phase (RP$i$), equiphase (EP$i$), and spiral phase (SP$i$) respectively, and $r_i^{\mathrm{or}}$, $r_i^{\mathrm{oe}}$, and $r_i^{\mathrm{os}}$ are the outer radii corresponding to the subphase, respectively. Furthermore, we define the ring length of RP$i$, EP$i$, and SP$i$ as $r_{\mathrm{rp}i}=r_i^{\mathrm{or}}-r_i^{\mathrm{ir}}$, $r_{\mathrm{ep}i}=r_i^{\mathrm{oe}}-r_i^{\mathrm{ie}}$, and $r_{\mathrm{sp}i}=r_i^{\mathrm{os}}-r_i^{\mathrm{is}}$, respectively, and $r_\mathrm{total}$ denotes the radius of the whole ASZP for convenience. Owing to the tight connection of these three annular phases, $r_i^{\mathrm{ie}}{=}r_i^{\mathrm{or}}$, and $r_i^{\mathrm{is}}{=}r_i^{\mathrm{oe}}$. Therefore, the radius of the whole ASZP$n$ is given by $r_\mathrm{total}=r_n^{\mathrm{os}}=r_1^{\mathrm{ir}}+r_{\mathrm{rp}1}+r_{\mathrm{ep}1}+r_{\mathrm{sp}1}+\cdots\cdots+r_{\mathrm{rp}n}+r_{\mathrm{ep}n}+r_{\mathrm{sp}n}$.

Figure 1 shows the process for generating TCPBs and the main features of TCPBs. It shows that the phase of TCPBs is formed by superposing ASZP$n$ onto the phase of circle Pearcey beams. The edges of the combined phase of ASZP and TCPBs are sharp (Figure 1), but they do not affect or reshape the AAF properties. For convenience, TCPBs with ASZP1 and ASZP2 are defined as TCPB1 and TCPB2, respectively. Thus, we can modulate TCPBs by altering one of the ASZP's parameters to explore the propagation properties and potential applications of TCPBs. However, it is difficult to derive the analytical solution of $E(r,\theta,z)$ from the Fresnel diffraction integral, (2+1)-dimensional potential-free Schrödinger equation eq. (1), and the corresponding initial solution eq. (2). Nevertheless, we can numerically simulate the propagation of TCPBs using the split-step Fourier transform method [40]. To spatially display the propagation patterns of TCPB1, we draw slice diagrams at certain propagation distances as shown in Figure 1(c). The beam is characterized by abrupt autofocusing, automatic generation of OBs, and self-rotation of the beam pattern, and the beamwidth of the beam decreases gradually during propagation until it approaches plane 4 where the beam starts to diffract. The beam is discussed in detail in a later section.

Herein, some parameters show little influence on the propagation dynamics of TCPBs. $l_i$ only reflects the number of vortex stripes of TCPBs. Besides, an increase in $\beta$ and $\gamma$ reduces only the peak intensity contrast of TCPBs with little contribution to the structure of TCPBs. $\alpha$ has no effect on the propagation properties. We choose appropriate values for these parameters to generate both high peak intensity contrast and high-quality TCPB. For convenience, we assume that $r_0=1.5$ mm, $r_1^{\mathrm{ir}}=0.1$ mm, $x_0=1$ mm, $A_0=1$, $p_\mathrm{s}=0.1$, $\eta=0.65$, $\xi=1$, $\beta=0.5\pi$, $\alpha=2\pi$, $\gamma=0$ unless otherwise specified.

### 2.2 Influence of the number of subphases

First, we simulated TCPB1 in free space (Figure 2). Both circle Pearcey beams and TCPB1 exhibit the AAF properties, as shown in Figure 2(a) and (c) [4]. To be specific, TCPB1 starts to undergo autofocusing several times at plane 1, but the intensity remains low at focal positions, such as planes 1,

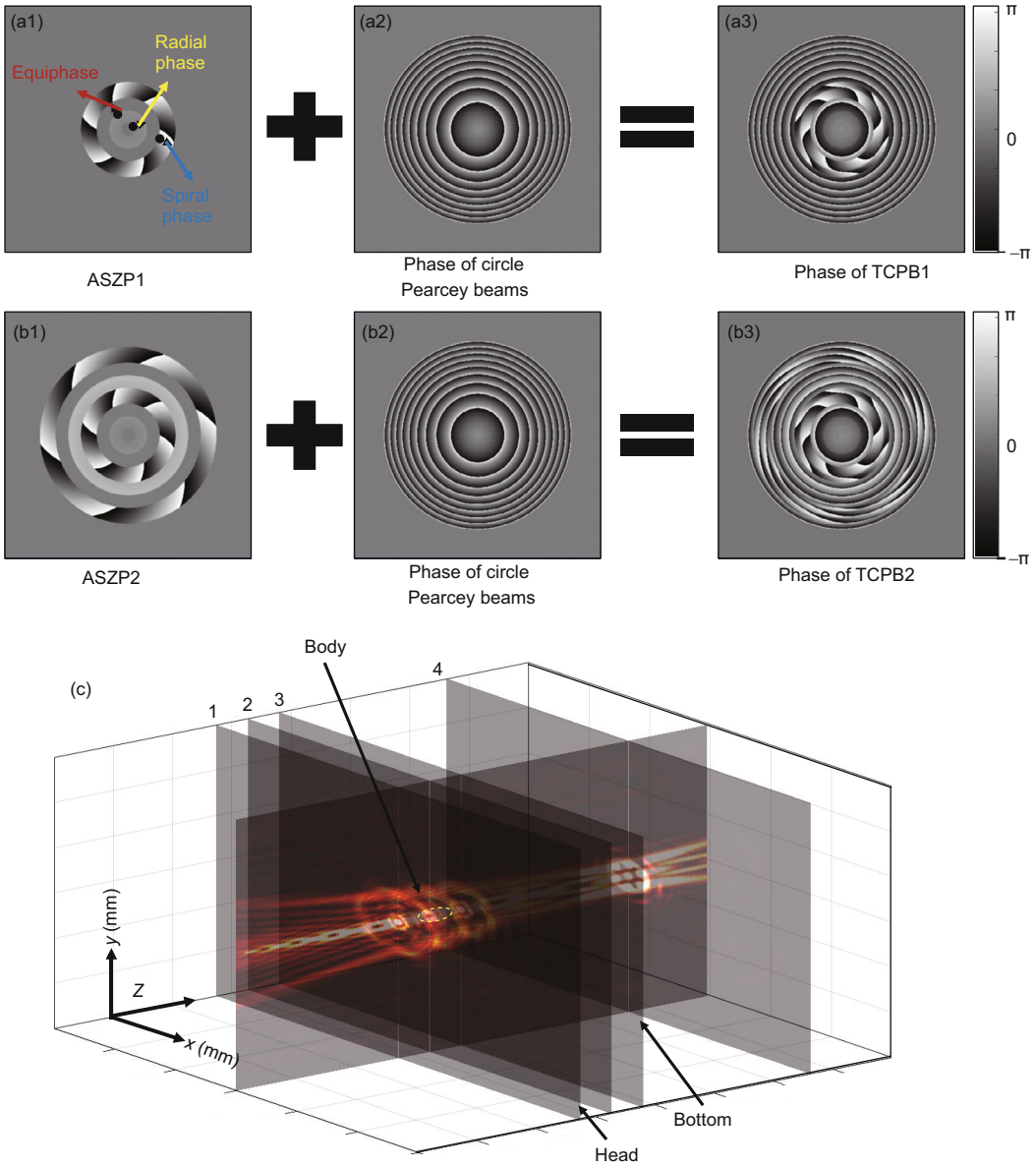


**Figure 1** (Color online) (a1)-(a3) Process for generating TCPB1; $l = 6, \beta = 0.5\pi$, $\alpha = 2\pi$, and $\gamma = 0$. (b1)-(b3) Process for generating TCPB2; $l_1 = 6$, $l_2 = 6$, $\beta = 0.5\pi$, $\alpha = 2\pi$, and $\gamma = 0$. (c) Slice diagram of TCPB1, illustrating 3D propagation dynamics numerically.

2, and 4, in contrast with plane 5, where the intensity abruptly increases by several orders of magnitude (Figure 2(c)). Compared with circle Pearcey beams [4], TCPB1 forms an on-axis OB on plane 3 where the low-intensity spot appears in the center of the transverse intensity pattern (Figure 2(b3)). On planes 2 and 3, TCPB1 focuses, and the main spots in the transverse intensity patterns form the head and bottom of the OB, respectively, implying that OB is generated. Besides, TCPB1 exhibits OAM because of the OV. These results prove that the TCPB1 has potential in particle manipulation [18-20]. In contrast to the doughnut transverse propagation mode of circle Pearcey beams, the transverse propagation mode of TCPB1 is a rotating (around the circumference) and twisting intensity distribution mode, which is similar to the pattern of a gear or a tornado. During the propagation, the spots initially slowly spin in a counterclockwise direction, after which the direction of rotation changes to clockwise at the AAF point due to the inversion of Pearcey beams [2,41], as is illustrated in Figure 2(b1)-(b6).

Next, the impact of the number of subphases on TCPBs is shown in Figure 3. TCPB2 imposes two subphases (ASZP2) that form two AAF points during propagation. OB is generated between the two focal points, as shown in Figure 3(a), which is even larger than that in Figure 2. Besides, Figure 3(c2) shows that the central part has low intensity instead of zero intensity. Additionally, the rotating property of

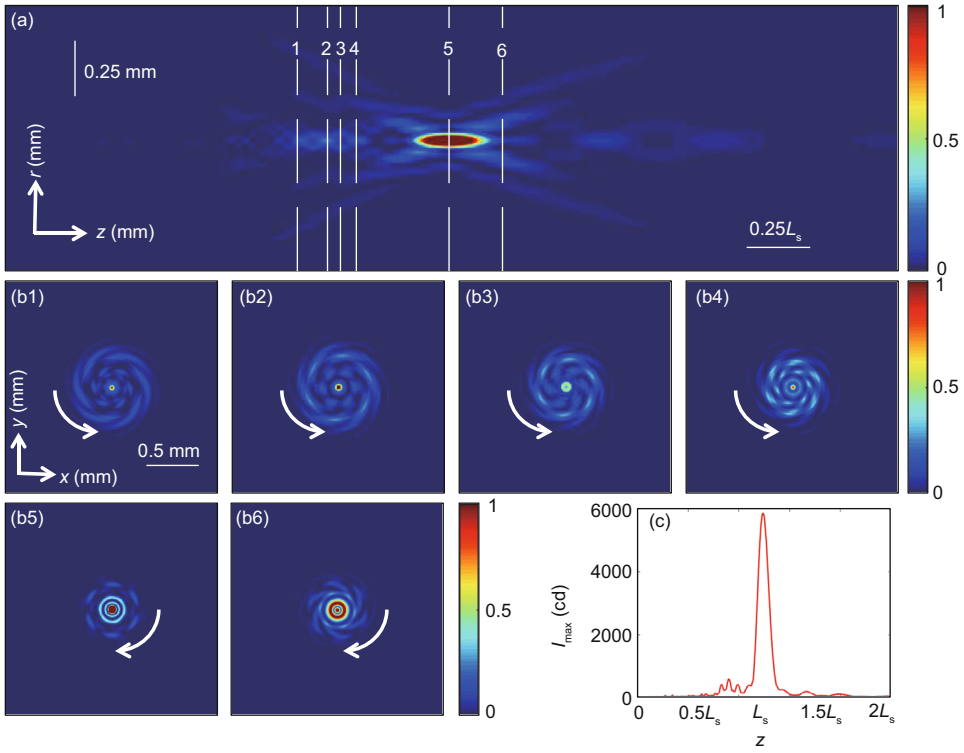


**Figure 2** (Color online) Numerical results showing the propagation of TCPB1 in free space with $p_s = 0.1$, $\beta = 0.5\pi$, $\alpha = 2\pi$, $l = 6$, $r_1^{ir} = 0.1$, $r_{rp1} = 0.2$, $r_{ep1} = 0.2$, and $r_{sp1} = 0.25$. (a) Side view of TCPB1 from the numerical beam propagation; (b1)-(b6) calculated transverse intensity patterns of TCPB1 at planes 1-6; (c) peak intensity of TCPB1 as a function of propagation distance $z$.

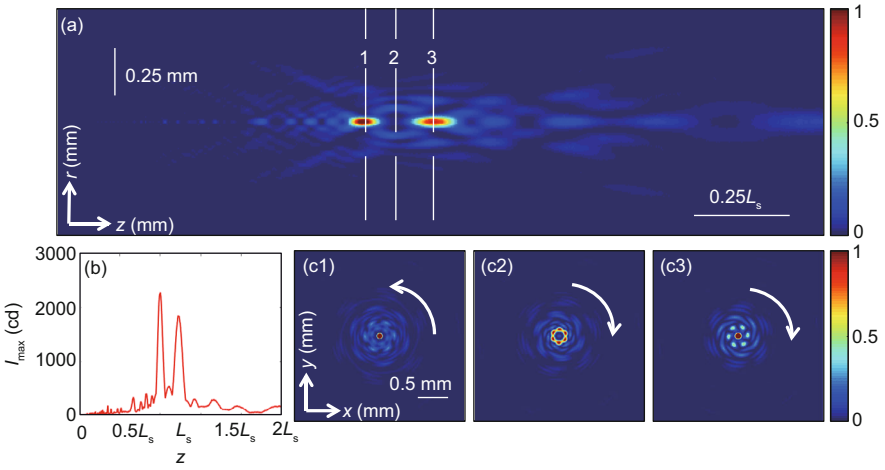


**Figure 3** (Color online) Propagation of TCPB2 in free space with $l_1 = 6$, $l_2 = 6$, $r_1^{ir} = 0.1$, $r_{rp1} = 0.2$, $r_{ep1} = 0.2$, $r_{sp1} = 0.25$, $r_{rp2} = 0.2$, $r_{ep2} = 0.2$, and $r_{sp2} = 0.25$. (a) Side view of TCPB2 from the numerical beam propagation; (b) peak intensity of TCPB2 as a function of propagation distance $z$; (c1)-(c3) calculated transverse intensity patterns of TCPB2 on planes 1-3. All other parameters are the same as those in Figure 2.

TCPB2 is almost identical to that of TCPB1. TCPB2 spins anticlockwise before approaching plane 1, as shown in Figure 3(c1). After plane 1, the transverse intensity pattern of TCPB2 rotates clockwise between planes 1 and 3, after which it changes again to anticlockwise rotation. Therefore, with the rotating property, the beam can be used as optical spanners to rotate particles. Compared with the polycyclic tornado ring Airy beams [38], TCPBs have high peak intensity contrast, as shown in Figures 2(c) and 3(b).

### 2.3 Influence of annular phases

An equiphase ($\gamma$) superposed on an annular spiral phase is equivalent to a vortex beam interfering with a plane wave

[42]. Besides, the vortex beam can be deflected by radial phases $\alpha r$ and $\beta r$ so that it interferes to a large extent with the plane wave [37]. Therefore, we analyze the influence of the radial phase, equiphase, and spiral phase on TCPBs. Figure 4 depicts the propagation of TCPB1 with different ring lengths of the radial phase. TCPB1 still has AAF properties, as shown in Figure 4(b1). With an increase in $r_{\mathrm{rp1}}$, the intensity scatters from the AAF point to the two focuses on both sides, and OB is generated. Moreover, OB is formed (illustrated in a white circle in Figure 4(a1)) before the AAF point. However, it is not well generated after the AAF point because there is no zero-intensity area near $L_{\mathrm{s}}$ in Figure 4(b2). When $r_{\mathrm{rp1}}$ increases to 0.7 mm, two OBs are generated, as indicated by the white circles in Figure 4(a2). Because of the ratio limit of the phase of TCPB1, when $r_{\mathrm{total}}$ increases to 1.45 mm, that is, the ring length of $r_{\mathrm{rp1}}$ approaches to 0.9 mm, OBs annihilate, as shown in the circle in Figure 4(a3). This phenomenon is discussed in detail in a later section. Therefore, the OBs are generated and annihilated with an increase in $r_{\mathrm{rp1}}$, and we can also obtain an appropriate number of OB by adjusting the radial phase $r_{\mathrm{rp1}}$.

Increasing the ring length of the equiphase enlarges the area of the plane wave, which enables the vortex beam to interfere better with the plane wave. Figure 5 shows the side views of TCPB1 with different ring lengths of the equiphase during the propagation. When the ring length of the equiphase is increased, the variation trends of propagation properties are similar to those of the radial phase. In particular, with an increase in $r_{\mathrm{ep1}}$, the intensity of the AAF point scatters to two sides, and two high-quality OBs are formed (Figure 5(a1)). When $r_{\mathrm{ep1}}$ is increased to 0.9 mm, the beam suffers weaker distortion (Figure 5(a2)) than that in Figure 4(a3).

Besides the equiphase and radial phase, the spiral phase $r_{\mathrm{sp1}}$ has a great impact on the propagation of TCPBs, as shown in Figure 6. Compared with Figure 2(a), the discrepancies of energy between the body and other parts of OB are more apparent, implying that high-quality multi OB is formed in Figure 6(a1). Through the simulation of TCPB1 with different $r_{\mathrm{sp1}}$, we found that the propagation character-

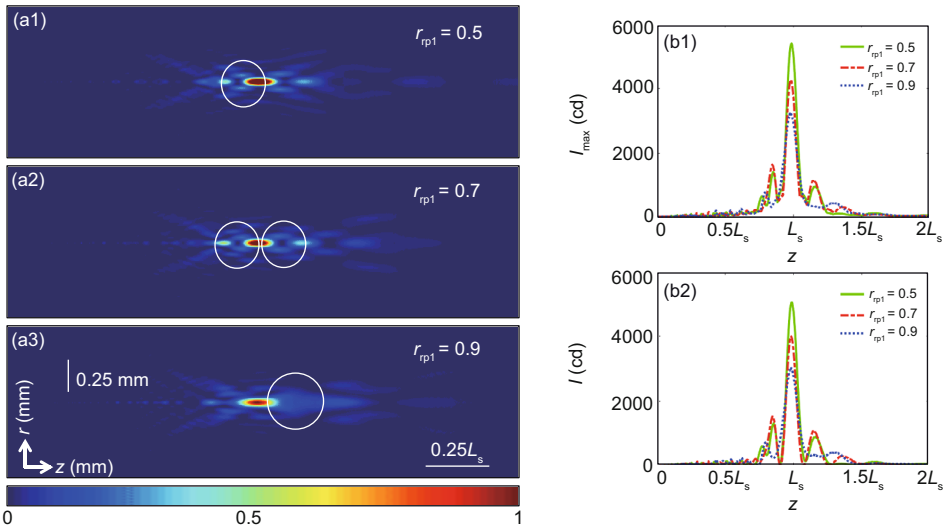


**Figure 4** (Color online) Propagation of TCPB1 in free space with different ring lengths of the radial phase $r_{\mathrm{rp1}}$ = 0.5, 0.7, and 0.9. (a1)-(a3) Side views of TCPB1 from the numerical beam propagation; (b1) peak intensity as a function of propagation distance $z$; (b2) on-axis peak intensity as a function of propagation distance $z$. All other parameters are the same as in Figure 2.

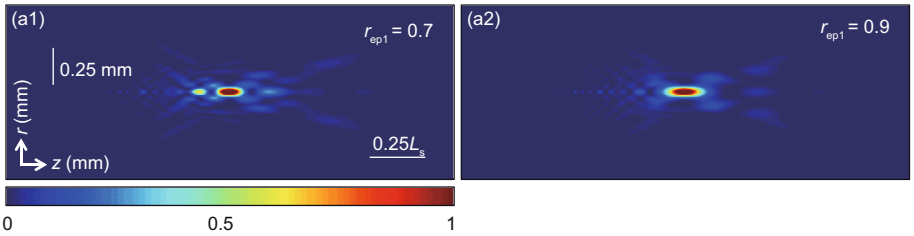


**Figure 5** (Color online) Propagation of TCPB1 in free space with different ring lengths of the equiphase $r_{\mathrm{ep1}}$ = 0.7 and 0.9. (a1), (a2) Side views of TCPB1 from numerical beam propagation. All other parameters are the same as in Figure 2.

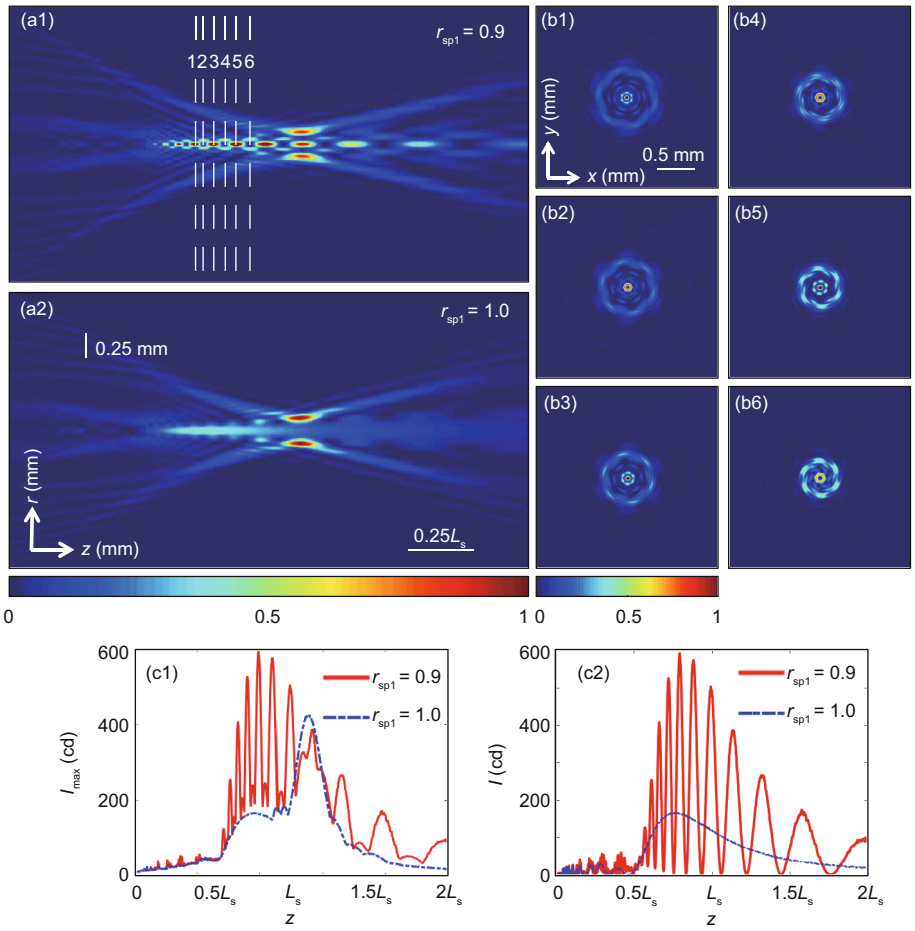


**Figure 6** (Color online) Propagation of TCPB1 in free space with different ring lengths of the spiral phase $r_{sp1}$ = 0.9 and 1.0. (a1), (a2) Side views of TCPB1 from numerical beam propagation; (b1)-(b6) calculated transverse intensity patterns of TCPB1 on planes 1-6; (c1) peak intensity as a function of propagation distance $z$; (c2) on-axis peak intensity as a function of the propagation distance $z$. All other parameters are the same as in Figure 2.

istics vary much when $r_{sp1}$ is more than 0.6, especially at $r_{sp1}$ = 0.9. Specifically, Figure 6(a1) shows that the beams undergo autofocusing back and forth more times than the above-mentioned beam, and several OBs are formed on the right part of the pattern. Interestingly, when $r_{sp1}$ reaches 1.0 mm, meaning that $r_{total}$ approaches the limit $r_0$ (1.5 mm), all OBs annihilate, and the intensity concentrates in two spots. In addition, Figure 6(c1) and (c2) show the generation and annihilation of OBs as well as the phenomenon of focusing several times. The occurrence of this phenomenon is explained in detail in a later section. Compared with the aforementioned parameters, the spiral phase $r_{sp1}$ has the greatest impact on TCPB1.

From the above results, the annihilation of OBs, that is, the distortion of the beam, occurs only when the radius of ASZP $r_{total}$ approaches 1.5 mm. The phenomenon can be explained by the phase distribution of the beam at the initial plane. Because $q(r)$, which is in the expression of initial light field of TCPBs, is in the role of the aperture and limits the special scale of the phase, annihilation occurs on the beam corresponding to Figure 7(a2), (a4), and (a6). In particular, when the outermost ring has phase singularities in the red circles in Figure 7(a2), (a4), and (a6), the phase singularities destroy the "phase barrier" and distort the beam. On the contrary, if no specific phase singularity exists, the OBs are not annihilated, as depicted in Figure 7(a1), (a3), and (a5). To verify our assumption, the outermost spiral phase in Figure 7(a6) is replaced with the radial phase $r_{rp2}$ = 0.1, resulting in a new phase distribution pattern (Figure 7(c)). Figure 7(b) shows the superior properties of TCPBs due to the protection of the outer barrier by the radial phase. Both the positions of focus shift and the number of OB are greater than those in Figure 6(a1). Hence, the appropriate superposition mode of ASZP enables the beam to gain diverse properties.

## 3 Experimental setup and results

Currently, it is more popular and convenient to control a phase [43] to implement a new type of light field. Since the

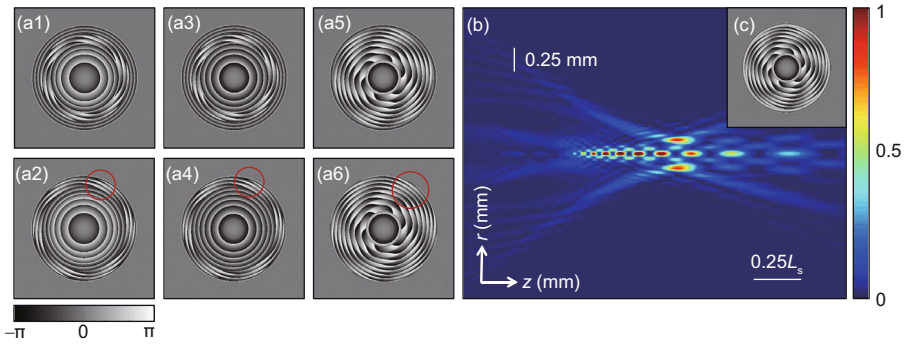


**Figure 7** (Color online) (a1), (a2) Phase distributions of TCPB1 with $r_{\mathrm{rp1}} = 0.7$ and 0.9, corresponding to the initial planes in Figure 4(a2) and (a3), respectively; (a3), (a4) phase distributions of TCPB1 with $r_{\mathrm{ep1}} = 0.7$ and 0.9, corresponding to the initial planes in Figure 5(a1) and (a2), respectively; (a5), (a6) phase distributions of TCPB1 with $r_{\mathrm{sp1}} = 0.9$ and 1.0, corresponding to the initial planes in Figure 6(a1) and (a2), respectively; (b) side view of TCPB from the numerical beam propagation with $l_1 = 6$, $l_2 = 6$, $r_1^{\mathrm{ir}} = 0.1$, $r_{\mathrm{rp1}} = 0.2$, $r_{\mathrm{ep1}} = 0.2$, $r_{\mathrm{sp1}} = 0.9$, and $r_{\mathrm{rp2}} = 0.1$; (c) phase distribution corresponding to the initial plane of (b). All other parameters are the same as in Figure 2.

liquid crystal SLM has the advantages of programmable, high resolution, and high diffraction efficiency, the pure phase modulation method of SLM is widely used for light-field modulation [44-46]. Herein, we generate TCPBs using the pure phase modulation method of SLM, as illustrated in the experimental system shown in Figure 8(a). An He-Ne laser is used to generate a linearly polarized Gaussian beam (632.8 nm) expanded and collimated by using BE. The beam is divided into two parts by BS: one is used as a reference beam, and the other is launched onto and reflected by the SLM (Santec SLM-200; pixel size 7.8/8.0 μm; pixel resolution (H)1900×(V)1200 pixels). To form TCPBs, we feed a "phase mask" (Figure 8(b1)) with interference fringes containing both phase and amplitude information of TCPBs [47] onto the SLM through a computer. The two above-mentioned beams interfere in the BS. In the $4f$ system, the beam performs Fourier and inverse Fourier transforms. Only the positive first diffracting order of the beam is selected by a spectral aperture to pass through the $4f$ filter system. Finally, TCPBs are generated at the focal plane of L2, and the intensity pattern of the beam can be observed in CCD (BeamPro 11.11; pixel size 5.5 μm; pixel resolution 2048×2048, 4.2 MPx), which is equivalent to the diffraction reproduction of the holography. The experimental and simulation results agree well at the initial plane (Figure 8(b2) and (b3)). In addition to the aforementioned method, beams can be generated using two SLMs to improve the diffraction efficiency of the beams [48].

The transverse intensity pattern at the initial plane is originally chosen by the phase mask in Figure 8(b1). However, the pattern significantly distorts during the propagation. Therefore, we modulate the transverse intensity pattern on the focal plane (plane 1 in Figure 2(a), plane 1 in Figure 3(a), and plane 1 in Figure 6(a1)) by the phase mask to compensate

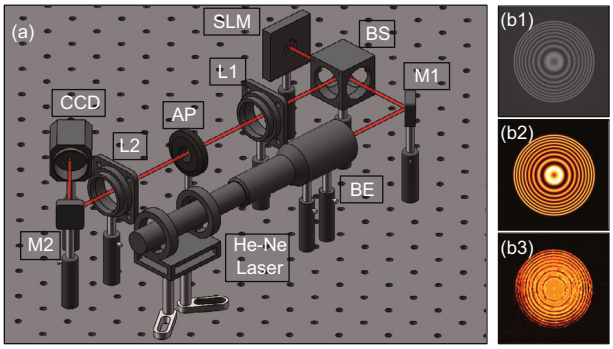


**Figure 8** (Color online) (a) Schematic diagram of the experimental setup for generating TCPBs. BE, beam expander; BS, beam splitter; M1 and M2, mirrors; L1 and L2, lenses; AP, aperture; SLM, spatial light modulator; CCD, charge-coupled device. (b1) Phase mask at the initial plane of the corresponding TCPB1 in Figure 2; (b2) corresponding calculated transverse intensity pattern; (b3) corresponding measured transverse intensity pattern.

for the distortion of the experimental results. Thus, nine measured transverse intensity patterns (Figure 9(b1)-(d3)) were obtained from the experiments. Figure 9(b1)-(c3) show that the rotation direction of the measured transverse intensity patterns agrees quite well with the inversion dynamics of the Pearcey beams. Besides, the measured transverse intensity patterns all have a hollow closed region in the center (Figure 9(b1), (c2), and (d2)). Therefore, the region forms an effective OB that can be used to trap and manipulate particles. Comparing the calculated and measured transverse intensity patterns, we find that the experimental results are consistent with the numerical simulation results.

## 4 Conclusions

In summary, we developed a scheme to design and generate TCPBs by active phase modulation using ASZP and exp-

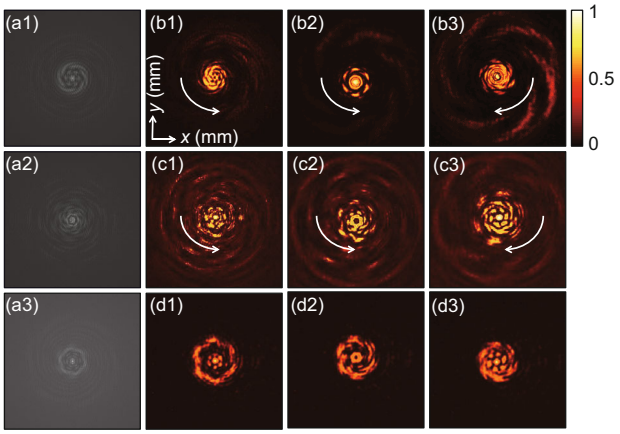


**Figure 9** (Color online) (a1)-(a3) Phase masks on plane 1 for the TCPBs in Figures 2(a), 3(a), and 6(a1), respectively; (b1)-(b3) experimentally recorded transverse intensity patterns on planes 3, 5, and 6, respectively, in Figure 2(a); (c1)-(c3) measured transverse intensity patterns on planes 1-3, respectively, in Figure 3(a); (d1)-(d3) measured transverse intensity patterns on planes 3-5, respectively, in Figure 6(a1).

erimentally generated the beams. We found that the focusing property of TCPBs can be modulated by the number of subphases and the superposition mode of ASZP. Besides, TCPBs can exhibit abrupt autofocusing once or multiple times in a sequence. In addition, TCPBs form one or more OBs in free space, indicating that TCPBs exhibit an unusual ability to trap particles. However, TCPBs have the self-rotation property of the beam pattern, which could be utilized for transferring OAM from beams to particles and for developing effective photonic tools for optical trapping and manipulation. For instance, with the properties exhibited by TCPBs, the beams can be used to rotate as an optical spanner to rotate particles. Furthermore, we conducted several numerical analyses and investigated the distortion phenomenon of TCPBs. Using the appropriate superposition mode of ASZP, we could explore the propagation properties of the beams. Owing to these properties, different types of TCPBs have application potentials in laser biomedical treatment, optical tweezers, optical communication, and optical spanners.

*This work was supported by the National Natural Science Foundation of China (Grant Nos. 11775083, and 11374108), the Science and Technology Program of Guangzhou (Grant No. 2019050001), the National Key R&D Program of China (Grant No. 2017YFA0303800), and the Special Funds for the Cultivation of Guangdong College Students' Scientific and Technological Innovation (Grant No. pdjh2020a0149).*

1 T. Pearcey, London Edinburgh Dublin Philos. Mag. J. Sci. **37**, 311 (1946).
2 J. D. Ring, J. Lindberg, A. Mourka, M. Mazilu, K. Dholakia, and M. R. Dennis, Opt. Express **20**, 18955 (2012).
3 M. V. Berry, and C. Upstill, Prog. Opt. **18**, 257 (1980).
4 X. Y. Chen, D. M. Deng, J. L. Zhuang, X. Peng, D. D. Li, L. P. Zhang, F. Zhao, X. B. Yang, H. Z. Liu, and G. H. Wang, Opt. Lett. **43**, 3626 (2018).
5 L. P. Zhang, D. M. Deng, X. B. Yang, G. H. Wang, and H. Z. Liu, Opt. Lett. **44**, 4654 (2019).
6 C. Sun, D. M. Deng, G. H. Wang, X. B. Yang, and W. Y. Hong, Opt. Commun. **457**, 124690 (2020).
7 L. Xin, Z. Q. Li, Y. E. Monfared, C. H. Liang, F. Wang, B. J. Hoenders, Y. J. Cai, and P. J. Ma, Opt. Lett. **46**, 70 (2021).
8 X. Y. Zhou, Z. H. Pang, and D. M. Zhao, Ann. Phys. **533**, 2100110 (2021).
9 N. K. Efremidis, and D. N. Christodoulides, Opt. Lett. **35**, 4045 (2010).
10 D. G. Papazoglou, N. K. Efremidis, D. N. Christodoulides, and S. Tzortzakis, Opt. Lett. **36**, 1842 (2011).
11 P. Zhang, J. Prakash, Z. Zhang, M. S. Mills, N. K. Efremidis, D. N. Christodoulides, and Z. G. Chen, Opt. Lett. **36**, 2883 (2011).
12 I. Chremmos, N. K. Efremidis, and D. N. Christodoulides, Opt. Lett. **36**, 1890 (2011).
13 N. K. Efremidis, V. Paltoglou, and W. von Klitzing, Phys. Rev. A **87**, 043637 (2013).
14 N. K. Efremidis, Z. G. Chen, M. Segev, and D. N. Christodoulides, Optica **6**, 686 (2019), arXiv: 1904.02933.
15 P. Panagiotopoulos, D. G. Papazoglou, A. Couairon, and S. Tzortzakis, Nat. Commun. **4**, 2622 (2013).
16 Y. F. Jiang, Z. L. Cao, H. H. Shao, W. T. Zheng, B. X. Zeng, and X. H. Lu, Opt. Express **24**, 18072 (2016).
17 R. S. Penciu, K. G. Makris, and N. K. Efremidis, Opt. Lett. **41**, 1042 (2016), arXiv: 1602.01602.
18 J. Arlt, and M. J. Padgett, Opt. Lett. **25**, 191 (2000).
19 N. Bokor, and N. Davidson, Opt. Commun. **279**, 229 (2007).
20 P. Zhang, Z. Zhang, J. Prakash, S. Huang, D. Hernandez, M. Salazar, D. N. Christodoulides, and Z. G. Chen, Opt. Lett. **36**, 1491 (2011).
21 B. P. S. Ahluwalia, X. C. Yuan, and S. H. Tao, Opt. Express **12**, 5172 (2004).
22 I. Chremmos, P. Zhang, J. Prakash, N. K. Efremidis, D. N. Christodoulides, and Z. G. Chen, Opt. Lett. **36**, 3675 (2011).
23 I. D. Chremmos, Z. G. Chen, D. N. Christodoulides, and N. K. Efremidis, Phys. Rev. A **85**, 023828 (2012).
24 X.-L. Wang, J. P. Ding, J.-Q. Qin, J. Chen, Y.-X. Fan, and H.-T. Wang, Opt. Commun. **282**, 3421 (2009).
25 X. Y. Weng, L. P. Du, P. Shi, and X. C. Yuan, Appl. Opt. **56**, 1046 (2017).
26 X. Y. Weng, L. P. Du, P. Shi, and X. C. Yuan, Opt. Express **25**, 9039 (2017).
27 Z. S. Man, Z. D. Bai, J. J. Li, S. S. Zhang, X. Y. Li, Y. Q. Zhang, X. L. Ge, and S. G. Fu, Appl. Opt. **57**, 3592 (2018).
28 L. Allen, M. W. Beijersbergen, R. J. C. Spreeuw, and J. P. Woerdman, Phys. Rev. A **45**, 8185 (1992).
29 K. T. Gahagan, and G. A. Swartzlander Jr., J. Opt. Soc. Am. B **16**, 533 (1999).
30 H. He, M. E. J. Friese, N. R. Heckenberg, and H. Rubinsztein-Dunlop, Phys. Rev. Lett. **75**, 826 (1995).
31 J. Y. Zhao, I. D. Chremmos, D. H. Song, D. N. Christodoulides, N. K. Efremidis, and Z. G. Chen, Sci. Rep. **5**, 12086 (2015).
32 S. H. Tao, X. C. Yuan, J. Lin, and Y. Y. Sun, J. Appl. Phys. **100**, 043105 (2006).
33 H. X. Ma, X. Z. Li, Y. P. Tai, H. H. Li, J. G. Wang, M. M. Tang, J.

Tang, Y. S. Wang, and Z. G. Nie, Ann. Phys. **529**, 1700285 (2017).
34 Y. S. Liang, S. H. Yan, M. R. He, M. M. Li, Y. N. Cai, Z. J. Wang, M. Lei, and B. L. Yao, Opt. Lett. **44**, 1504 (2019).
35 Y. J. Shen, X. J. Wang, Z. W. Xie, C. J. Min, X. Fu, Q. Liu, M. L. Gong, and X. C. Yuan, Light Sci. Appl. **8**, 90 (2019).
36 J. C. Ni, C. W. Wang, C. C. Zhang, Y. L. Hu, L. Yang, Z. X. Lao, B. Xu, J. W. Li, D. Wu, and J. R. Chu, Light Sci. Appl. **6**, e17011 (2017), arXiv: 1608.01220.
37 Y. P. Lan, Y. X. Qian, and Z. J. Ren, Ann. Phys. **532**, 1900530 (2020).
38 Y. Wu, C. J. Xu, Z. J. Lin, H. X. Qiu, X. M. Fu, K. H. Chen, and D. M. Deng, New J. Phys. **22**, 093045 (2020).
39 N. Gao, C. Q. Xie, C. Li, C. S. Jin, and M. Liu, Appl. Phys. Lett. **98**, 151106 (2011).
40 T.-C. Poon, and T. Kim, *Engineering Optics with Matlab* (World Scientific, Singapore, 2006).
41 X. Y. Zhou, Z. H. Pang, and D. M. Zhao, Opt. Lett. **45**, 5496 (2020).
42 H. X. Ma, X. Z. Li, Y. P. Tai, H. H. Li, J. G. Wang, M. M. Tang, Y. S. Wang, J. Tang, and Z. G. Nie, Opt. Lett. **42**, 135 (2017).
43 V. Bagnoud, and J. D. Zuegel, Opt. Lett. **29**, 295 (2004).
44 M. S. Chen, S. J. Huang, W. Shao, and X. P. Liu, Appl. Phys. B **123**, 215 (2017).
45 D. M. Deng, Y. M. Gao, J. Y. Zhao, P. Zhang, and Z. G. Chen, Opt. Lett. **38**, 3934 (2013).
46 Z. J. Ren, C. F. Ying, H. Z. Jin, and B. Chen, J. Opt. **17**, 105608 (2015).
47 I. S. V. Yepes, T. A. Vieira, R. A. B. Suarez, S. R. C. Fernandez, and M. R. R. Gesualdi, Opt. Commun. **437**, 121 (2019).
48 Z. H. Pang, X. Y. Zhou, Z. L. Liu, and D. M. Zhao, Phys. Rev. A **102**, 063519 (2020).